Chin. Phys. Lett. **39**, 062901 (2022)

Development of Time-of-Flight Polarized Neutron Imaging at the China Spallation Neutron Source

Ahmed Salman[1,2,3], Jianrong Zhou(周健荣)[1,2,3], Jianqing Yang(杨建清)[1,2,4], Junpei Zhang(张俊佩)[1,2], Chuyi Huang(黄楚怡)[1,2,3], Fan Ye(叶凡)[1,2,5], Zecong Qin(秦泽聪)[1,2], Xingfen Jiang(蒋兴奋)[1,2], Syed Mohd Amir[1,2], Wolfgang Kreuzpaintner[1,2], Zhijia Sun(孙志嘉)[1,2], Tianhao Wang(王天昊)[1,2*], and Xin Tong(童欣)[1,2*]

[1]*Institute of High Energy Physics, Chinese Academy of Sciences, Beijing 100049, China*
[2]*Spallation Neutron Source Science Center, Dongguan 523803, China*
[3]*University of Chinese Academy of Sciences, Beijing 100049, China*
[4]*Xi'an Research Institute of Hi-Tech, Xi'an 710025, China*
[5]*College of Materials Science and Engineering, Chongqing University, Chongqing 400044, China*

(Received 7 March 2022; accepted 6 May 2022; published online 29 May 2022)

A time-of-flight polarized neutron imaging setup was realized by integrating an *in situ* pumped polarized ^{3}He spin filter and energy dispersive neutron camera on the neutron technique development beamline (BL-20) of the China Spallation Neutron Source (CSNS). Test experiments were performed with a solenoid with aluminum wire as a sample. These demonstrated that polarized radiography with a field of view in diameter 2.0 cm at different wavelengths can be obtained. The wavelength-dependent polarization was used to distinguish the neutron polarization behavior for different positions inside and outside the solenoid. The results of this work show the possibility of applying the technique at CSNS and marks a milestone for future polarized neutron imaging developments.

DOI: 10.1088/0256-307X/39/6/062901

Polarized neutron imaging (PNI) has experienced a rapid development and increase in applications in recent years.[1,2] The most prominent applications include studying the Meissner effect of superconductors,[3,4] the trapped magnetic field in superconductors,[5] the skin effect in the bulk of electrical conductors,[6] magnetic phase transitions,[7] and magnetic field distribution in electric devices such as transformers and motors.[8,9]

The behavior of the polarization of a neutron beam in a magnetic field $\boldsymbol{B}$ can classically be described via the neutron's magnetic moment which experiences a torque that causes a Larmor precession $\omega_{\rm L}$. The corresponding precession angle ϕ reads[3]

$$\phi = \omega_{\rm L} t = \frac{\gamma}{v}\int \boldsymbol{B}\cdot d\boldsymbol{l} = \frac{\gamma m\lambda}{h}\int \boldsymbol{B}\cdot d\boldsymbol{l}, \qquad (1)$$

where t is the traveling time of a neutron along a path $\boldsymbol{l}$ in the magnetic field, γ is the neutron gyromagnetic ratio, h is the Planck's constant, and m, v, and λ denote the mass, velocity, and wavelength of the neutron, respectively.

For PNI, the incident neutron beam is polarized and its polarization is analyzed after the interaction with the sample. If a sample alters the polarization, the measured intensities will also be altered due to the filtering effect of the analyzing device located after the sample.[1] To realize this experimentally, typically a combination of a solid state polarizer before the sample, which polarizes the incoming beam, and a polarized ^{3}He neutron spin filter (NSF)[10,11] as an analyzer after the sample is used. The neutron polarization analysis is based on measuring the intensity of transmitted neutrons for both states, in which the analyzer selectively filters spin-up or spin-down neutrons. The polarization of the neutron beam reads

$$P = \cos\phi = \frac{I_{\rm up} - I_{\rm down}}{I_{\rm up} + I_{\rm down}}, \qquad (2)$$

where $I_{\rm up}$ and $I_{\rm down}$ denote the measured transmitted intensity for spin-up and spin-down states, respectively.

This neutron polarization analysis method can be combined with neutron imaging methods into PNI to visualize the spatial distribution of magnetic fields for different magnetic materials and electric devices. It provides two-dimensional radiography or three-dimensional tomography imaging and reflects the influence of magnetic field components along the neutron beam path onto the polarization vector of the neutron.[1,3]

According to Eq. (1) the precession angle ϕ is directly proportional to the wavelength. Hence, if a time-of-flight (ToF) neutron detector with sufficient time resolution is applied, any pulsed polychromatic neutron beam can be utilized for PNI and the mag-

*Corresponding authors. Email: wangtianhao@ihep.ac.cn; tongxin@ihep.ac.cn
© 2022 Chinese Physical Society and IOP Publishing Ltd

netic field distribution for a magnetic sample can be mapped as a function of neutron wavelength.[1,12]

The wavelength dependence of the measured polarization allows adiabatic transition, non-adiabatic transition, precession and depolarization to be distinguished.[1,13] In the case of a significantly large magnetic field component perpendicular to the neutron polarization vector, an oscillatory behavior in the wavelength-dependent polarization is expected to occur [Eq. (1)]. Therefore, the absolute quantity of the final polarization rotation and the magnetic field strength can be obtained even if multiple precession occurs.[1,13] Ultimately, arbitrarily orientated magnetic fields could also be mapped via a polarimetric approach in which the polarization of the incoming and outgoing beams can wavelength dependently be manipulated and analyzed.[1,14,15]

In contrast to ToF PNI, monochromatic PNI requires a neutron beam of a well-defined wavelength as the accumulated precession angle [Eq. (1)] is wavelength dependent. An imperfect monochromatic beam can result in multiple precessions that lead to dephasing of the neutron polarization and a full depolarizing of the neutron beam.[16] The precession of neutron polarization is indistinguishable from an additional rotation by 2π or π that can cause losing information of the final total orientation of a polarization vector.[1,13] In addition to this, the obtained images from a monochromatic neutron beam measures the polarization changes induced by a magnetic field only with respect to a single direction of the initial neutron polarization. Differing neutron polarization behaviors cannot be distinguished.[1] Therefore, a single PNI measurement requires a certain priori knowledge of the sample magnetic field before performing PNI experiment to avoid the phase wrapping of polarization vector rotations beyond π angle.[1]

PNI using monochromatic neutron beams is highly developed and implemented at continuous neutron sources.[4,5,7,17] PNI with (pulsed) white neutron beams, as they are intrinsic to spallation neutron sources, poses however certain challenges, which result from the ToF analysis of the neutron beam.[1,8,9,12] To realize ToF PNI with its own advantages, dedicated instruments are needed to carefully monitor and control the polarization vector, such as the availability of ToF neutron detectors with sufficient time resolution, and an optimization of the neutron polarization and transmittance for energy-resolving PNI. This allows visualizing the magnetic field distribution for a magnetic sample as a function of neutron wavelength and opens the door for even potentially revolutionary improvements for mapping the magnetic field of various magnetic materials and electric devices.

Here we report on realizing energy-resolving PNI capabilities and their feasibility at CSNS as one of the major pulsed neutron sources.

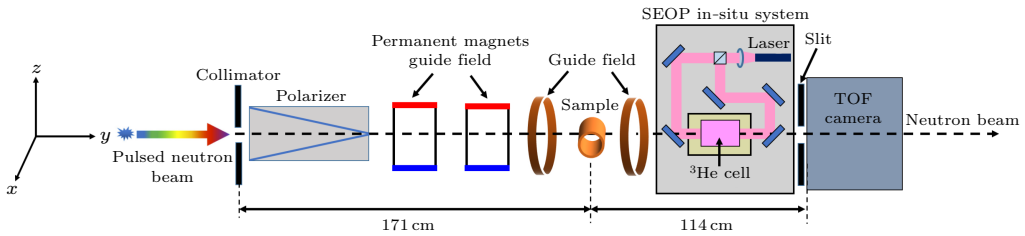

Fig. 1. Schematic illustration of the time-of-flight polarized neutron imaging setup at beamline BL-20.

Table 1. Summary of the basic parameters of the polarized neutron imaging setup at beamline BL-20.

Wavelength range	$1.0 \leq \lambda \leq 5.5$ Å
Field of view	2.0 cm in diameter
Collimation ratio (L/D)	85.5
Neutron beam intensity (at 100 kW)	8.8×10^5 s^{-1}
Sample-to-detector distance	114 cm
Imaging detector system	Energy resolving neutron imaging detector[18]

Polarized Neutron Imaging Setup. An energy dispersive PNI setup was realized on the Neutron Technology Development Beamline (BL-20) at the CSNS. At the time of the experiment (viz. CSNS operating at 100 kW), a collimated neutron beam with a diameter of $D = 2.0$ cm provided an intensity of 8.8×10^5 s^{-1} in the wavelength band of $1.0 \leq \lambda \leq 5.5$ Å. A schematic of the setup is shown in Fig. 1. The neutron beam path is along the y-axis. Beam polarization parallel to the z-axis was achieved using a polarizing V-cavity after the initial circular collimation slit. The polarization was maintained using permanent magnet based guide field elements that provided a magnetic field of > 10 G in the z-direction followed by electromagnetic coils which adiabatically rotate and maintain the neutron polarization along the y-axis. An in-house developed *in situ* pumped ^{3}He NSF system[19–21] was applied to analyze the beam polarization after its interaction with the magnetic field of the sample.

As a demonstration sample, a solenoid with alu-

minum wire of 6.0 cm length, 1.5 cm radius, wire diameter of 0.15 cm, and with 37 windings was used. The solenoid axis was parallel to the x-axis to generate a uniform magnetic field in a direction that is perpendicular to both the neutron path and the polarization vector. It was placed at a distance of $L = 171$ cm after the collimation slit. The solenoid was mounted such that the neutron beam passes through its upper edge as described in Fig. 2. For the measurements a direct current of 5.0 A was applied to the solenoid. An energy resolving neutron imaging detector[18] was placed behind the analyzer with a solenoid-to-detector distance of 114 cm to record two-dimensional images with corresponding detection time stamps. A circular slit of 2.0 cm diameter in front of the detector for removing diffusely scattered neutrons, completed the collimation. The setup provided a collimation ratio $L/D = 85.5$, and a field-of-view diameter 2.0 cm. The ^{3}He polarization of the NSF along the y-axis could be reversed using an adiabatic fast passage AFP-NMR method.[22,23] This allowed neutron images to be recorded for the spin-up and spin-down neutron states. The data accumulation time was 1.0 h for each spin state. The basic parameters of the PNI set up at beamline BL-20 are summarized in Table 1.

Results and Discussion. The data for both spin states were acquired simultaneously based on the recorded neutron ToF using the energy resolving neutron imaging detector. A data reduction process, including a background subtraction, noise suppression, data rebinning, statistical processing, and polarization analysis, was applied, after which the polarization images and polarization curves as a function of neutron wavelength were generated. Within the applied wavelength range of $1.0 \leq \lambda \leq 5.5$ Å, 90 detector images with $\Delta\lambda = 0.05$ Å were obtained. The field of view covers the upper part of the solenoid and a region above it as depicted in Fig. 2. To improve the counting statistics, the intrinsic detector resolution was reduced to an effective pixel size of 0.014×0.014 cm^2 by binning four neighboring detector channels in a 2×2 raster into one.

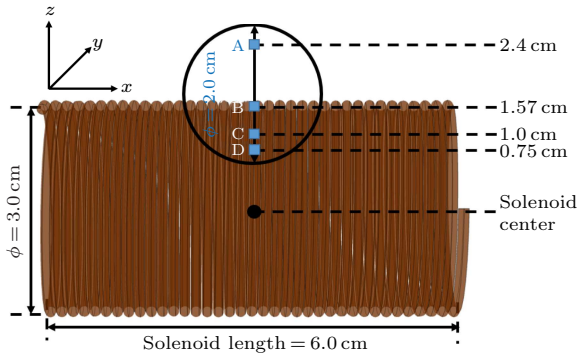

Fig. 2. A sketch of the sample with the circular irradiated region. A, B, C, and D represent four characteristic points of interest at different distances from the center of the solenoid.

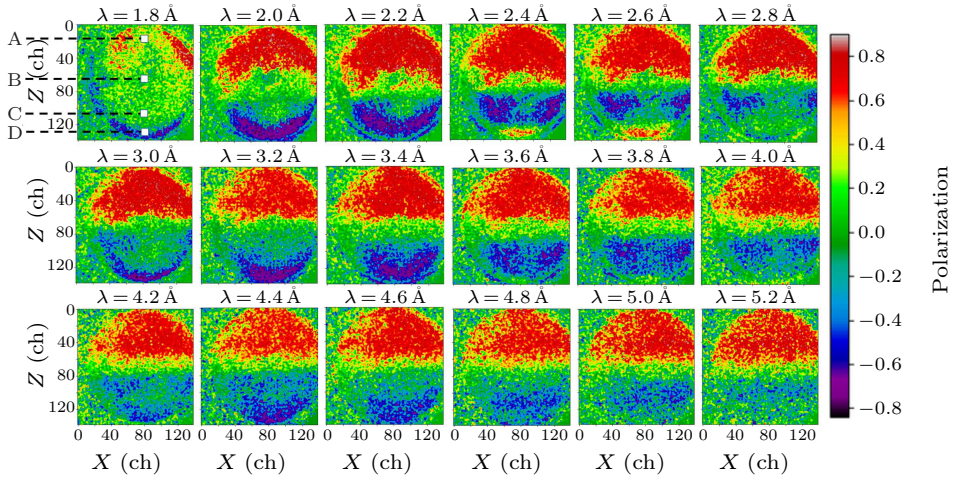

Fig. 3. Polarization images at some different wavelengths. The circle in the images represents the irradiated area defined by a circular slit placed in front of the ToF camera. The four relevant positions (A, B, C, and D) used for analysis are shown on the image at $\lambda = 1.8$ Å.

Polarization images as a function of wavelength (Fig. 3) were obtained from the measured spin-up and spin-down intensities $I_{\rm up}$ and $I_{\rm down}$, respectively, using Eq. (2). The red color in the upper half of the irradiated circle in Fig. 3 corresponds to the part of the polarized neutron beam that does not undergo any precession but an adiabatic transition. The polarization values at the lower half of the illuminated circular area are wavelength dependent and indicate the existence of a significant magnetic field component which is perpendicular to the neutron polarization vector, corresponding to a non-adiabatic transition.

To support data analysis, the magnetic fields generated by the electromagnetic coils (i.e., the guide field components) and the solenoid were simulated using the finite element method (FEM) software COMSOL Multiphysics®.[24] This simulation provides insight into the magnetic field distribution in and outside of

the solenoid. The electromagnetic coils generate an essentially uniform magnetic field in y-direction that guides the neutron polarization. The magnetic flux density in the xy and yz planes, intersecting the center of the solenoid, are shown in Fig. 4. Based on the magnetic field simulation results, we identified four relevant positions for our analysis of which each position has different magnetic field characteristics: one outside the solenoid (position A), one on the very edge of the solenoid (position B), and two inside the solenoid (positions C and D). For these positions the neutron polarization behavior as a function of wavelength was analyzed. The magnetic field components along the y-axis at positions A, B, C, and D (see Fig. 2) are given in Fig. 5. For position A, where the field components perpendicular to the polarization vector are negligible, the polarization is conserved, as is directly evident from the adiabatic transition of the neutron polarization. For position B the magnetic field is arbitrarily oriented. This causes the neutron beam through this region to depolarize. Positions C and D are regions with a significant magnetic field component B_x perpendicular to the polarization vector. Here the polarization vector will precess around the non-zero components of the perpendicular magnetic field. Note that for positions C and D the magnetic field components B_x have different field path integrals as the path length inside the solenoid is decreasing with the distance from the center. This allows a comparison of the oscillatory behavior in the wavelength dependent precession for different integral field path lengths within the solenoid to be performed.

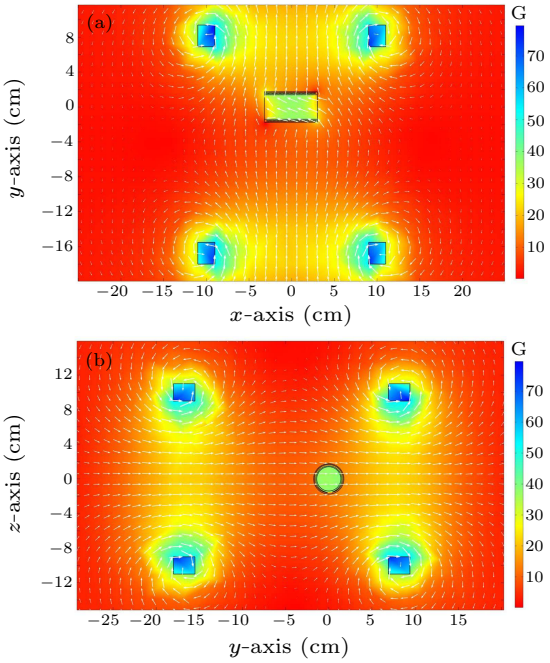

Fig. 4. Magnetic field simulation for the solenoid and the electromagnetic guide field coils: (a) xy plane view at $z = 0$, (b) yz plane view at $x = 0$. The simulation shows a uniform magnetic field in y-direction that preserves the neutron polarization.

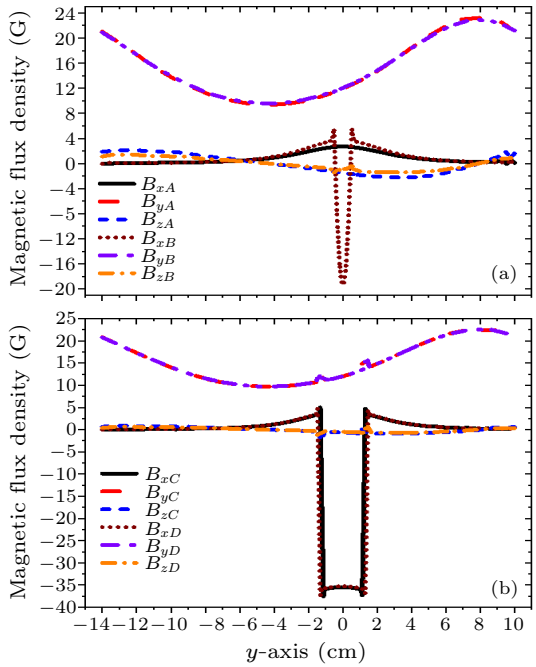

Fig. 5. Simulated magnetic field components for (a) $(B_{\mathrm{xA}}, B_{\mathrm{yA}}, B_{\mathrm{zA}})$, $(B_{\mathrm{xB}}, B_{\mathrm{yB}}, B_{\mathrm{zB}})$, and (b) $(B_{\mathrm{xC}}, B_{\mathrm{yC}}, B_{\mathrm{zC}})$ and $(B_{\mathrm{xD}}, B_{\mathrm{yD}}, B_{\mathrm{zD}})$ at positions A, B, C, and D, respectively.

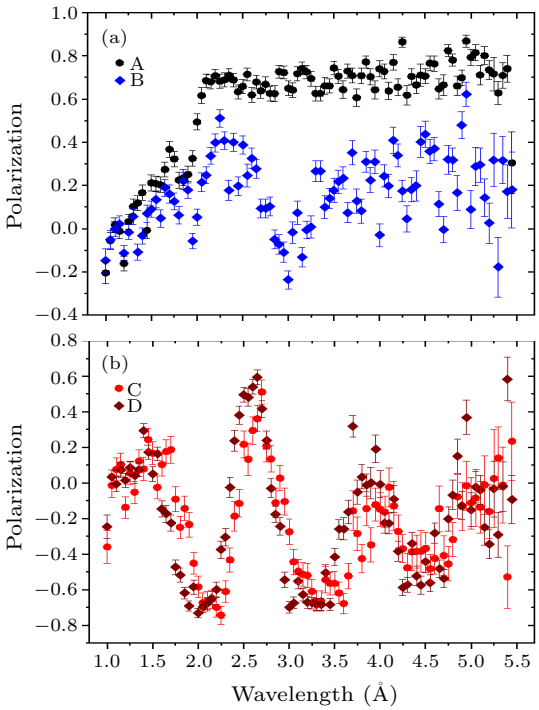

Fig. 6. Neutron polarization as a function of wavelength at the positions: (a) A and B, (b) C and D, as defined in Fig. 2.

The polarization as a function of wavelength at the four selected positions A, B, C, and D is given in Fig. 6. At position A only the characteristic polarization powers of the polarizer and analyzer influence the neutron beam. The polarization values below the lower cut-off wavelength of the V-cavity of 2.0 Å are rather limited

and it is also visible that with increasing wavelength the data generally becomes more noisy as the precession angle is increasingly affected by the remaining small magnetic stray fields outside the solenoid. The polarization values at position B are scattered highly for wavelengths above 3.5 Å, which corresponds to a de-polarization of the neutron beam that results from a combination of arbitrarily oriented magnetic fields and the stray magnetic field. However, an oscillatory behavior is visible for wavelengths below 3.5 Å. If looking at positions C and D, the wavelength-dependent polarization shows an oscillatory behavior over the full wavelength range, which is the result of the precession of the neutron polarization around the perpendicular magnetic field component created by the solenoid. Nevertheless, also for these points, the polarization values show an increasing distortion of the precession angle by magnetic stray fields as the wavelength increases. If comparing the polarization spectra at positions C and D with each other, they both exhibit a similar trend in the oscillatory behavior. The oscillating frequency is, however, slightly shifted to shorter wavelengths for position D as the neutron path length through the solenoid is longer, which results in an increasing number of rotations of the neutron polarization. The damping in the oscillation curves for positions C and D with increasing wavelength results from the influence of the magnetic stray fields, the beam divergence and a not ideal spatial resolution due to the small collimation ratio and the large sample-detector distance.

The oscillatory behavior in the polarization as a function of wavelength is a proof of the neutron polarization vector precession around the non-zero component of the perpendicular magnetic field and a characteristic observable feature when neutron beams are wavelength-dependently analyzed for PNI.

In summary, it is realized that we can successfully record two-dimensional polarized neutron images and we can apply the relevant data analysis algorithms for extracting and resolving the neutron polarization at different positions of a sample.

Further upgrades for PNI are ongoing, which include improved instrumental components, optimized polarized neutrons transfer, increases in the spatial resolution, and the addition of a magnetic field shielding around the sample. These improvements are expected to allow magnetic field distributions of various magnetic samples to be visualized with a quality that will allow PNI at CSNS to be developed into a tomography technique for complex magnetic structures.

Acknowledgment. This research was initiated and supported by the National Key Research and Development Program of China (Grant No. 2020YFA0406000) and the National Natural Science Foundation of China (Grant No. 11875265). Implementing the ^{3}He spin filter on the experiment was developed under the Scientific Instrument Developing Project of the Chinese Academy of Sciences (Grant No. ZDKYYQ20190004). Development of the superconducting instrument used in this work was supported by the National Natural Science Foundation of China (Grant Nos. 12075265 and U2032219). The magnetic field simulation and analysis work were supported by the Guangdong Natural Science Funds for Distinguished Young Scholar. We give special thanks to the support of Dr. Songlin Wang on the deployment of the instrumentation on BL-20, and Dr. Zackary Buck for his effort on setting up the beamline.

References

[1] Strobl M, Heimonen H, Schmidt S, Sales M, Kardjilov N, Hilger A, Manke I, Shinohara T and Valsecchi J 2019 *J. Phys. D* **52** 123001
[2] Hilger A, Manke I, Kardjilov N, Osenberg M, Markötter H and Banhart J 2018 *Nat. Commun.* **9** 4023
[3] Kardjilov N, Manke I, Strobl M, Hilger A, Treimer W, Meissner M, Krist T and Banhart J 2008 *Nat. Phys.* **4** 399
[4] Wang T, Jiang C, Bilheux H *et al.* 2019 *Rev. Sci. Instrum.* **90** 033705
[5] Ţuţueanu A E, Sales M, Eliasen K *et al.* 2020 *Physica C* **575** 1353691
[6] Manke I, Kardjilov N, Strobl M, Hilger A and Banhart J 2008 *J. Appl. Phys.* **104** 076109
[7] Kardjilov N, Hilger A, Manke I, Strobl M and Banhart J 2018 *J. Imaging* **4** 23
[8] Hiroi K, Shinohara T, Hayashida H, Parker J D, Oikawa K, Harada M, Su Y and Kai T 2017 *J. Phys.: Conf. Ser.* **862** 012008
[9] Hiroi K, Shinohara T, Hayashida H, Parker J, Su Y, Oikawa K, Kai T and Kiyanagi Y 2018 *Physica B* **551** 146
[10] Gentile T R, Nacher P, Saam B and Walker T 2017 *Rev. Mod. Phys.* **89** 045004
[11] Gainov R, Mezei F, Füzi J and Russina M 2019 *Nucl. Instrum. Methods Phys. Res. Sect. A* **930** 42
[12] Shinohara T, Kai T, Oikawa K *et al.* 2020 *Rev. Sci. Instrum.* **91** 043302
[13] Strobl M, Kardjilov N, Hilger A, Penumadu D and Manke I 2011 *Nucl. Instrum. Methods Phys. Res. Sect. A* **651** 57
[14] Sales M, Strobl M, Shinohara T, Tremsin A, Kuhn L T, Lionheart W R, Desai N M, Dahl A B and Schmidt S 2018 *Sci. Rep.* **8** 2214
[15] Sales M, Shinohara T, Sørensen M K, Knudsen E B, Tremsin A, Strobl M and Schmidt S 2019 *J. Phys. D* **52** 205001
[16] Dawson M, Manke I, Kardjilov N, Hilger A, Strobl M and Banhart J 2009 *New J. Phys.* **11** 043013
[17] Kardjilov N, Hilger A, Manke I, Woracek R and Banhart J 2016 *J. Appl. Crystallogr.* **49** 195
[18] Yang J, Zhou J, Jiang X *et al.* 2021 *Nucl. Instrum. Methods Phys. Res. Sect. A* **1000** 165222
[19] Zhang J, Huang C, Qin Z *et al.* 2022 *Sci. Chin. Phys. Mech. Astron.* **65** 241011
[20] Qin Z, Huang C, Buck Z N, Kreuzpaintner W, Amir S M, Salman A, Ye F, Zhang J, Jiang C, Wang T and Tong X 2021 *Chin. Phys. Lett.* **38** 052801
[21] Huang C, Zhang J, Ye F, Qin Z, Amir S M, Buck Z N, Salman A, Kreuzpaintner W, Qi X, Wang T and Tong X 2021 *Chin. Phys. Lett.* **38** 092801
[22] Babcock E, Petoukhov A, Chastagnier J *et al.* 2007 *Physica B* **397** 172
[23] Ino T, Arimoto Y, Shimizu H M *et al.* 2012 *J. Phys.: Conf. Ser.* **340** 012006
[24] https://cn.comsol.com/products 2022 *COMSOL Multiphysics®*